

OPTICAL AND INFRARED SENSOR FUSION FOR HYPERVELOCITY ASTEROID INTERCEPT GUIDANCE

Joshua Lyzhoft*, Dalton Groath[†], and Bong Wie[‡]

In this paper we investigate the technical feasibility of a new terminal guidance system architecture for a hypervelocity asteroid intercept vehicle (HAIV). All previous terminal guidance system studies for an asteroid intercept problem have mainly considered optical cameras due to their cost-effective nature and acceptable target tracking performance as was demonstrated by Deep Impact mission. However, this paper examines a concept of blending optical and infrared (IR) sensors for reliable target tracking and robust intercept of small (50 -150 m) asteroids. A preliminary design study for developing a reference 50-kg class IR sensor system for a 1000-kg class HAIV is described, and the intercept performance of a closed-loop terminal guidance system employing both optical and IR sensors is demonstrated.

INTRODUCTION

The Asteroid Deflection Research Center (ADRC) at Iowa State University has been developing a Hypervelocity Asteroid Intercept Vehicle (HAIV) concept against the most probable impact threat of asteroids with short warning time [1–3]. An illustration of the proposed HAIV terminal intercept scenario is provided in Figure 1. A scaled polyhedron model of 433 Eros was used in [4] for a closed-loop optical navigation and guidance simulation study of the HAIV concept.

Expanding upon the study results in [1–4], we propose a new terminal guidance system architecture for intercepting asteroids. All previous terminal guidance system studies for an asteroid intercept problem have considered mainly optical cameras due to their cost-effective nature and acceptable target tracking performance as was demonstrated by Deep Impact mission. However, we consider a blended use of optical and infrared (IR) sensors for reliable target tracking and robust hypervelocity intercept of small (50 -150 m) asteroids. For such technically challenging, hypervelocity intercept missions to be successful, both optical and IR sensors need to be considered.

The terminal guidance system employing optical cameras tracks the center of brightness (COB) of a target asteroid. This system becomes ineffective if the target asteroid is not sufficiently illuminated by the sun, or if the sun-asteroid-spacecraft phase angle is near 180 degrees. However, an IR sensor will be able to provide target information required for onboard guidance algorithms even when optical cameras cannot. An IR sensor, with proper wavelength band corresponding to the target asteroid's temperature, will be able to detect and track the target asteroid. A blended optical and IR sensor system will allow for targeting of the center of figure (COF), which for some cases is near

*Graduate Research Assistant, Asteroid Deflection Research Center, Department of Aerospace Engineering

[†]Undergraduate Research Assistant, Asteroid Deflection Research Center, Department of Aerospace Engineering

[‡]Vance Coffman Endowed Chair Professor, Asteroid Deflection Research Center, Department of Aerospace Engineering, Iowa State University, Ames, IA 50011

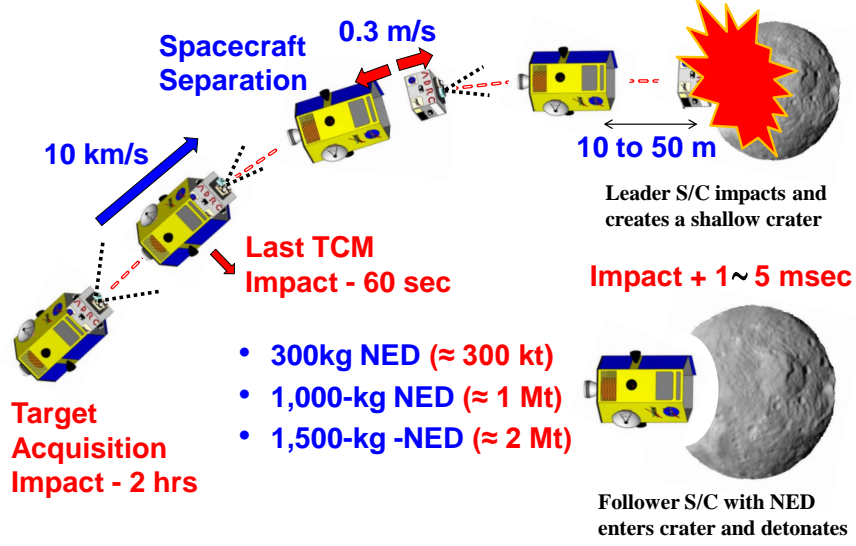


Figure 1. A baseline terminal intercept scenario of a two-body HAIV carrying a nuclear explosive device (NED) [1–3].

to the center of mass (COM) of the target body. Impacting closer to the the target COM will ensure best results for target fragmentation [5]. Preliminary design of a reference 50-kg class IR sensor system for a 1000-kg class HAIV will be described, and the intercept performance of a closed-loop terminal guidance system employing the optical and IR sensor fusion will be demonstrated in this paper.

3D POLYHEDRON MODEL

This section addresses the rendering of the images in simulation memory that correspond to camera data to be processed by the interceptor spacecraft. We begin with a triangulation of surface points represented as a 3D wireframe polygon model. The target model is derived from data for the asteroid 433 Eros collected by the NEAR mission, and it has 200,700 faces [6]. This number of faces corresponds to the variable n_f of the computer model. Generally, the number of vertices needed to fill out the model, n_v , is strictly less than n_f , so it is more computationally efficient to do calculations on the vertices where possible. However, much of our information depends in some sense on an orientation of the body surface, for which the faces are necessary. A connectivity array stores the relationships between each set of vertex data and which face it applies to. If \mathbf{R}_1 , \mathbf{R}_2 , and \mathbf{R}_3 are the position vectors for the vertices of a face, as shown in Figure 2, then we have \mathbf{X}_i , \mathbf{Y}_i , and \mathbf{Z}_i for $a \leq i \leq n_f$, defined as

$$\mathbf{X}_i = \mathbf{R}_2 - \mathbf{R}_1, \quad \mathbf{Y}_i = \mathbf{R}_3 - \mathbf{R}_1, \quad \mathbf{Z}_i = (\mathbf{R}_1 + \mathbf{R}_2 + \mathbf{R}_3) / 3 \quad (1)$$

The unit normal vectors of each face are calculated and stored as

$$\mathbf{N}_i = \mathbf{X}_i \times \mathbf{Y}_i, \quad \mathbf{N}_i \cdot \mathbf{Z}_i > 0 \quad (2)$$

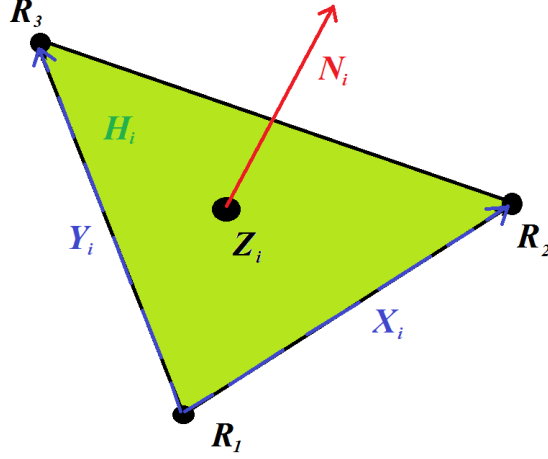


Figure 2. Facet geometry definitions.

The wireframe model uses a known rotation state of the target, though this information is not available to the spacecraft. A rotation matrix is applied to the initial conditions so that a simulated “real” state is known for the 3D model. To complete this system description, we require a unit sun vector, $\hat{\mathbf{S}}$, in the direction of the sun from the target and a unit view vector, $\hat{\mathbf{V}}$, in the direction of the spacecraft from the target. We assume that the true center of mass of the target is at the origin on this coordinate system.

Camera Pointing and Focus Plane

In order to decouple the attitude and translation mechanics of the present simulation system, a “perfect” pointing was adopted for the camera. Thus, the choice of estimated center of mass or previously computed center of brightness is at the center of the camera focal plane, with the camera needing zero time to adjust to the new settings. Modifications to this scheme, including integration with spacecraft attitude are expected to be conducted in the near future.

The camera focal plane distance was chosen arbitrarily as the distance from the spacecraft to target. Since this plane is perpendicular to $\hat{\mathbf{V}}$ we can project the 3D model onto this plane by subtracting the component along this vector, thus the projected locations of the vertices are described by

$$\mathbf{P}_j = \mathbf{R}_j - \hat{\mathbf{V}}, \quad 1 \leq j \leq 3 \quad (3)$$

To save computational time and storage space, a condensed array of these values are computed only for the faces satisfying $\mathbf{N}_i \cdot \hat{\mathbf{V}} > 0$. This results in only the faces visible to the spacecraft. Due to the decoupling of the camera dynamics, a direct orientation of this plane is not possible given the currently available information. Thus, a direction for camera “up” must be chosen. We choose unit vectors $\hat{\mathbf{U}}$ and $\hat{\mathbf{V}}$ such that

$$\hat{\mathbf{W}} = \hat{\mathbf{S}} \times \hat{\mathbf{V}}, \quad \hat{\mathbf{U}} = -\hat{\mathbf{V}} \times \hat{\mathbf{W}} \quad (4)$$

Therefore, the sunlight will always come into frame from a horizontal direction, and “up” will always be orthogonal to the plane containing the target, the sun, and the spacecraft. The coordinates

Table 1. Simulated camera parameters

	High Resolution	Medium Resolution	Infrared
Resolution $x_r \times y_r$ (pixels)	1024×1024	1024×1024	512 x 512
Field of View f_v (radians)	2.05×10^{-3}	10.0×10^{-3}	10.0×10^{-3}
Pixel Size at 1,000 km (m)	2.0	9.8	19.5

of each vertex in this plane can be computed as

$$\tilde{\mathbf{P}}_j = [u_j \ w_j]^T = [\mathbf{P}_j \cdot \hat{\mathbf{U}} \quad \mathbf{P}_j \cdot \hat{\mathbf{W}}]^T \quad (5)$$

At this point, what is visible to the spacecraft depends on camera parameters that interpret the “real” system. The resolution and field of view for the cameras simulated are listed in Table 1. At each time step, these are used to compute the half resolution of the image plane, R_h . If \mathbf{R}_T is the position vector representing the spacecraft in the target frame, then this can be computed as

$$R_h = |\mathbf{R}_T| \tan \left(\frac{1}{2} f_v \right) \quad (6)$$

where f_v represents the field of view in radians (assumed isotropic). If x_r and y_r represent the x and y resolutions in the camera 2D pixel frame, then the information represented by each pixel corresponds to a size of $2R_h/x_r$ in the horizontal direction and $2R_h/y_r$ in the vertical direction.

Illumination Conditions

A simple flat shading model is used to calculate the brightness of the target surface. Given a diffuse lighting coefficient, k_d , and an ambient lighting coefficient, k_a , the corresponding brightness attributed to each face of the 3D model is computed as

$$C_{optical,i} = \begin{cases} k_d (\mathbf{N}_i \cdot \hat{\mathbf{S}}) + k_a & \text{if } \mathbf{N}_i \cdot \hat{\mathbf{S}} > 0 \\ 0 & \text{if } \mathbf{N}_i \cdot \hat{\mathbf{S}} \leq 0 \end{cases} \quad (7)$$

where a value $C_{optical,i}$ of 1 corresponds to perfect reflectivity of the incident sunlight at that distance. A greyscale colormap is used for human visualization. The diffuse coefficient works closely in line with the albedo, and is chosen to be 0.25 for the simulations. Since the cameras we are using have very little time to resolve detail of the body, we assume that their lower threshold for brightness is very low and therefore $k_a = 0$.

For the IR model, the fictional face illumination can be described by

$$C_{IR,i} = k_{d_{IR}} (\mathbf{N}_i \cdot \hat{\mathbf{S}}) + k_{a_{IR}} \quad (8)$$

where $k_{d_{IR}}$ represents the heating of the asteroid by the sun, and $k_{a_{IR}}$ is the constant coefficient that corresponds to the core temperature of the asteroid. For both face coefficients, this model is very fast and can be computed completely in parallel for each face.

When additional lighting detail is desired, the following interpolation model due to Gouraud [7] is used. Let each vertex have a normal $\tilde{\mathbf{N}}_1$, $\tilde{\mathbf{N}}_2$, and $\tilde{\mathbf{N}}_3$ computed as an average of the adjacent faces,

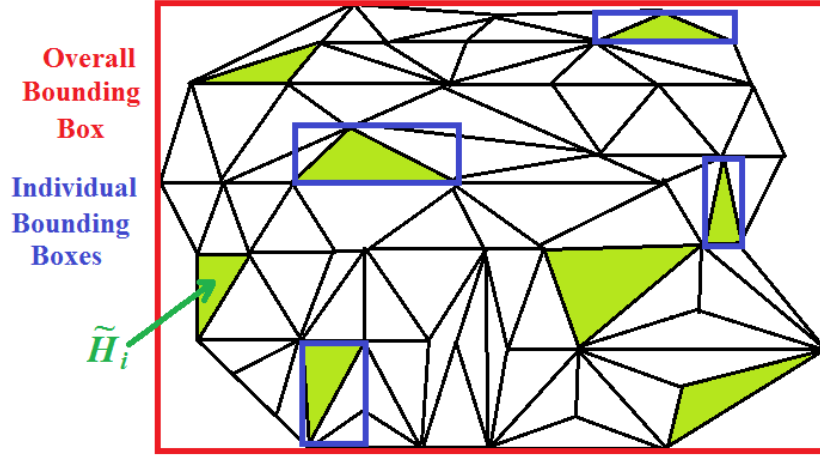


Figure 3. Parallel trim reduction technique.

found from inverting the connectivity array. Then, a corresponding value for brightness at each vertex \tilde{C}_1 , \tilde{C}_2 , and \tilde{C}_3 is computed using the flat shading model equation. If a pixel representing the image plane at $[u \ w]^T$ is calculated to intercept this triangle, then an inverse squared weighted average is assigned to the pixel, as follows:

$$C(u, w) = \frac{\alpha_1}{\alpha_T} \tilde{C}_1 + \frac{\alpha_2}{\alpha_T} \tilde{C}_2 + \frac{\alpha_3}{\alpha_T} \tilde{C}_3 \quad (9)$$

where $\alpha_T = \alpha_1 + \alpha_2 + \alpha_3$ and

$$\alpha_j = \frac{1}{(u - u_j)^2 + (w - w_j)^2} \quad \text{for } 1 \leq j \leq 3 \quad (10)$$

Pixel Value Assignment

For either the flat or interpolated shading models, the facet at which a pixel intercepts the target projection must be determined. This is done on the GPU (graphics processing unit) computer in parallel to reduce computational time, especially using a higher fidelity target model. Each pixel is assigned to coordinates in the (u, w) plane representing the center of the box over which the pixel is integrated. This works well when the size of a pixel is on the scale of the surface facets, but an averaged value needs to be used at greater distances. To determine the intercepted triangle, we first compute the upper and lower bounds of each visible triangle in parallel. Then, a reduction is performed to get the outer limits of the target in the (u, w) plane. This process is represented in Figure 3. Pixels outside of this range can automatically be assigned a value of 0. In fact, only the location and value of nonzero image components are stored in the present computational model.

The arrays containing the limits of each facet are sorted, and then a scan of these arrays is completed. This lets us assign a vector of possible intersections for each pixel. This vector contains the IDs of all facets through which the pixel passes through the bounding box. This is generally a low number. For each candidate intersection, the convex hull of the triangle, H_i , is identified, as shown in Figure 2. This is projected onto the (u, w) plane, forming the set \tilde{H}_i shown in Figure 3. If \tilde{X}_i

and $\tilde{\mathbf{Y}}_i$ are the projections of \mathbf{X}_i and \mathbf{Y}_i in the (u, w) plane, then the coordinates of the pixel can be expressed as

$$\begin{bmatrix} u \\ w \end{bmatrix} = \tilde{\mathbf{P}}_1 + d_1 \tilde{\mathbf{X}}_i + d_2 \tilde{\mathbf{Y}}_i \quad (11)$$

which can be viewed as a transformation into the affine system defined by these two vectors. It is a well-known result from geometry that the point $[u \ w]^T$ lies within the triangle if $d_1 > 0$, $d_2 > 0$, and $d_1 + d_2 < 1$. This generally assigns a single facet as the possibility for intersection. However, at pixels near the boundary of the target, several potential intersection may occur. In these cases, the closest triangle (largest $\mathbf{Z}_i \cdot \hat{\mathbf{V}}$) is chosen.

Line-of-Sight Vector

For the present implementation, the estimated line-of-sight vector is chosen to be the center of brightness. If $I(u, w)$ is the value of brightness for each image element, then the centroid of the image array is computed using an weighted average, as follows:

$$\bar{u} = \frac{\sum I(u_i, w_i) u_i}{\sum I(u_i, w_i)}, \quad \bar{w} = \frac{\sum I(u_i, w_i) w_i}{\sum I(u_i, w_i)} \quad (12)$$

The line-of-sight vector in the spacecraft frame is obtained as

$$\mathbf{\Lambda} = \begin{bmatrix} \bar{u} \\ \bar{w} \end{bmatrix} - \mathbf{R}_T \quad (13)$$

IR SIGNAL-TO-NOISE RATIO (SNR) ESTIMATION

The IR detector array receives signals from the asteroid, and the sensor array wells are filled. While the signal is obtained from the asteroid, the detector also has noise and dark current values, which is said to be total detector noise. Since the frequencies of this noise are unknown, the approximation for the signal-to-noise ratio (SNR) is computed. Once the value of the SNR reaches a mission selected value, the object in question, here an asteroid, is said to be able to be detected. To simulate these values, approximation of blackbody radiation signal current and noise signal current are calculated.

Signal Analysis

A step in approximating the asteroid signal requires the integration of Planck's law over the detectable wavelength band of the IR detector. Black body radiation for different temperature values is shown in Fig. 4. The form of Planck's law used here is a function of the wavelength. While there are multiple bands for the wavelengths, the focus here is on objects that are in the 250 Kelvin range [8]. For this case, the wavelengths being used start at the Mid Infrared N band ($7.5 - 14.5\mu\text{m}$) and extend to $16.5\mu\text{m}$, which is used for the W3 band given for the WISE telescope in section 3, number 2, Table 1 [9]. This gives radiance of the asteroid with integration bounds as

$$L = \int_{\lambda_1}^{\lambda_2} \epsilon \frac{2hc}{\lambda^5} \frac{1}{e^{\frac{hc}{k_b T_{ast} \lambda}} - 1} d\lambda \quad (14)$$

Definitions of numerous symbols appearing in this section are summarized in Notation section of this paper.

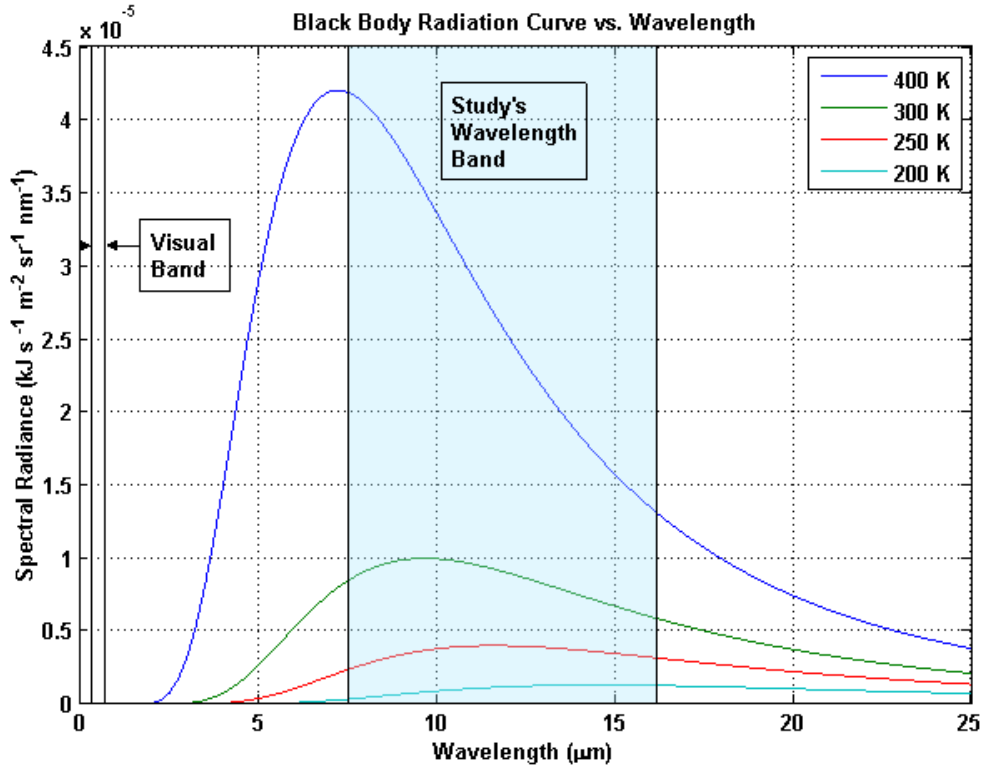


Figure 4. Black body radiation for different temperature values.

Once the radiance is found, the irradiance on the detector can be calculated. This takes into account the solid angle subtended by a circular approximation of the asteroid. The irradiance is then given by

$$E = \frac{L\pi r_{ast}^2}{d_{ast}^2} \quad (15)$$

To calculate the signal current, the irradiance needs to be converted into a photon flux. This will compute the minimum amount of electrons passing through the aperture. The Wein's displacement law for finding the wavelength of peak emission is given by

$$\lambda_{max} = b/T_{ast} \quad (16)$$

where λ_{max} is the maximum energy per photon, in Joules, and

$$\psi = \frac{hc}{\lambda_{max}} \quad (17)$$

The photon flux, which is the amount of photons passing through one square meter, can be determined by dividing the irradiance by the maximum energy per photon at the desired wavelength. This gives the photon flux as

$$\Phi = \frac{E}{\psi} \quad (18)$$

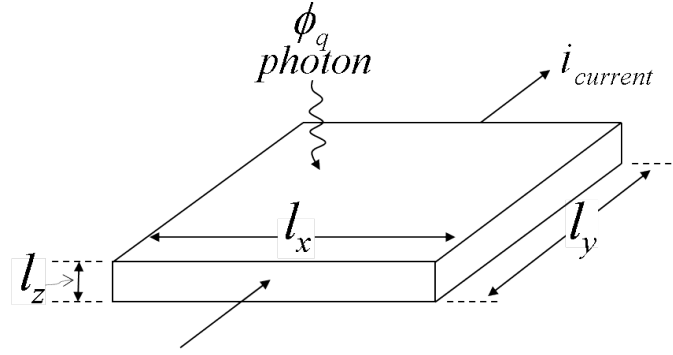


Figure 5. A diagram showing the various characteristics of the detector.

Given in Amperes, the current of the signal can then be found by finding the number of photons passing through the area of the aperture multiplied by charge of an electron and device specific parameters. This equation is given by Rieke [11] as

$$I_{signal} = (\Phi \pi r_{ap}^2 \tau_{optics}) q \eta G \quad (19)$$

The variable τ_{optics} is estimated to be at 0.504 in the optical by Schott [10]. This is assumed to be the transmission coefficient in the IR range as well.

Noise and Dark Current Analysis

One of the most important aspects of signal processing is the amount of noise in the system. If there is too much noise and the noise signal is not known, it would be virtually impossible to differentiate from correct or incorrect data. The following analysis incorporates four places there could be unwanted current added to the system. This, for generality, will be called a noisy current.

Dark Current. To more completely analyze the performance of a detector, the dark current of the system must be calculated as

$$I_{dark} = n_{e,d} n_{pix} q \quad (20)$$

It should be noted that dark current is not noise, but has a combination of signal and noise. In this paper, this current will be assumed to be unwanted and considered as noise. Testing the detector is the best way to obtain the dark current electron per pixel value. The number of electrons per pixel per second, $n_{e,d}$, is given to be approximately 5 for the 1024×1024 pixel silicon-arsenide detector used for the W3 band of the WISE [12].

Johnson Noise. Another source of a noisy current is given by the Johnson noise, which includes the resistance of the detector. This noise, from Dereniak and Boremann [13], is described by

$$I_J = \sqrt{\frac{4k_B T_d \Delta f}{(\rho l_y)/(l_x l_z)}} \quad (21)$$

As a general guideline, Teledyne suggests the the thickness of a HgCdTe layer in the detector should be at least the cutoff wavelength to ensure high quantum efficiency of the material [14]. From Figure 2 in a paper by Morin and Miata [15], it is illustrated that the conductivity of silicon doped with arsenic (n-type) at an impurity concentration of $20 \times 10^{18} \text{ cm}^{-3}$ is approximately 1

$(\text{Ohm/m})^{-1}$ [15]. The temperature of the Silicon Arsenide, given by the WISE telescope detector, is approximately 7.8 kelvin [12].

The Electronic bandwidth of the detector is approximated by Schneider and Liu [16] as

$$\Delta f = \frac{1}{2\tau_{int}} \quad (22)$$

By replacing Δf the Johnson noise current equation takes the new form as

$$I_J = \sqrt{\frac{2k_B T_d}{\frac{\rho_{ly}}{l_x l_z} \tau_{int}}} \quad (23)$$

Shot Noise. Shot noise is the noise generated by random incidence of photons on the detector surface. This equation is given by Dereniak and Boreman [13] as

$$I_S = \sqrt{2q\bar{I}\Delta f} \quad (24)$$

The average current \bar{I} is taken to be the current generated by the signal.

Generation-Recombination Noise. Generation-Recombination noise is the noise as the result of the generation and recombination of charged particles within the detector material [13]. The expression given by Dereniak and Boreman [13] is given by

$$I_{GR} = 2qG\sqrt{\eta\Phi\tau_{optics}A_d\Delta f} \quad (25)$$

SNR Formulation

Since the signal current and the noisy current have been obtained, the SNR can be calculated. The noisy currents are uncorrelated, which means they add quadratically. This follows from the definition of uncorrelated noise as the sum of the separate noise powers, as follows:

$$I_N = \sqrt{I_{dark}^2 + I_J^2 + I_S^2 + I_{GR}^2} \quad (26)$$

With this, the final SNR is then determined as the ratio of the signal power to the noise power. Here the resistance is assumed the same and the SNR is described by

$$SNR = \frac{I_{signal}^2}{I_N^2} \quad (27)$$

The SNR is being used to calculate at what distance the asteroid can be seen. With a high SNR, the asteroid would be easy detected compared to lower SNR, where the object would be skewed, blurred, etc.

INFRARED MAGNITUDE

At long distances from the target, the asteroid will radiate IR signal much like how a star would in visible light. The magnitude of the asteroid can be estimated by using the wavelength of an emission, denoted by λ . Here, the peak emission wavelength is used. By using the black body

Table 2. Exoplanet information given by Pederson [17]

Exoplanet	Distance from Earth (ly)	Equilibrium Temperature (K)	Radius (R_{\oplus})	N Band (mag)	Visual Band (mag)
Gliese 581c	~20.22	327	1.53	15.0	25.7
Gliese 581d	~20.22	177	1.71	17.0	28.1

emission frequency equation (Planck's Law), the radiance of the object at maximum frequency can be found. This equation is given by

$$B(v) = \frac{2hv^3}{c^2} \frac{1}{e^{\frac{hv}{k_B T}} - 1} \quad (28)$$

For this case, the temperature of the respective body is represented by the T parameter. For the radiance to be calculated, the variable v is defined as

$$v = c/\lambda \quad (29)$$

Flux density is needed of a reference body and the asteroid. Once both of these are obtained, the magnitude of the asteroid can be found. The general flux density is given by

$$F_{object} = B(v) \pi \frac{r_{object}^2}{d_{object}^2} \quad (30)$$

Once the flux density is calculated for both the reference body and the asteroid in question, the magnitude of the reference body, for the N band, must be obtained. The reference object being used is Gliese 581c, which is located in the Libra constellation. Since at great distances, the object can use the general formula for star magnitude as a function of the flux density given by

$$m_{ast} = m_{Gliese581c} - 2.512 \log_{10} \left(\frac{F_{ast}}{F_{Gliese581c}} \right) \quad (31)$$

Table 2 gives simulated characteristics of the reference exoplanet, along with another object in this star system. An exoplanet or other asteroids are excellent reference objects due to their frequency of maximum emission (correlation to body temperature). The last column in this table, for comparison, shows what both of these celestial objects would appear like in the visual band of light.

RESULTS

While the specific guidance algorithms are not discussed in this paper, closed-loop guidance simulations have been conducted. Figure 6 Shows what the image of the asteroid looks at the beginning, impact minus 2 hours, of the terminal guidance phase of the mission using the IR sensor. As can be seen, the asteroid appears much like a star in the visual band of light. The majority, is in fact, emitting in the N band of mid infrared, corresponding to the stars appearance in Table 3. This table shows the corresponding SNR values for various asteroid and aperture diameters at 84000 km from the target.

From Table 3, if an asteroid with a diameter of 50 meters is desired to be observed with an SNR of approximately ten, it can be seen that an aperture size of 13.7 centimeters would suffice. This,

Table 3. SNR at a distance of 84,000 km from target asteroid

Aperture Diameter (m)/ Asteroid Diameter (m)	0.0522	0.0944	0.137	0.179	0.200
50	2.11E-01	2.26	9.9	29	45.4
150	17.1	1.83E+02	8.02E+02	2.35E+03	3.68E+03
500	3.09E+03	3.31E+04	1.45E+05	4.26E+05	6.65E+05
1000	3.38E+04	3.61E+05	1.58E+06	4.65E+06	7.26E+06

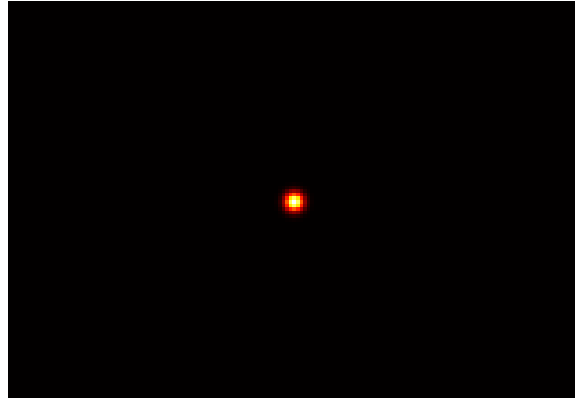


Figure 6. IR image depiction of a 150-m diameter asteroid at a distance of 84,000 km.

however, does not show insight on choosing focal length or other parameters, such as sensor dwell time.

Figure 7 depicts what the asteroid will potentially look like at close ranges without the observation of heat radiation. A comparison of the optical and the fictional IR images is provided in Figure 8. As can be seen, the pink plus, which is either the center of figure (IR) or the center of brightness (optical), is much closer to the center of mass for the IR model. The center of mass is illustrated by the blue circle. Running the computer program with the heating radiation effect takes much longer than that with only the optical observation.



Figure 7. Fictional IR model without heat radiation effects.

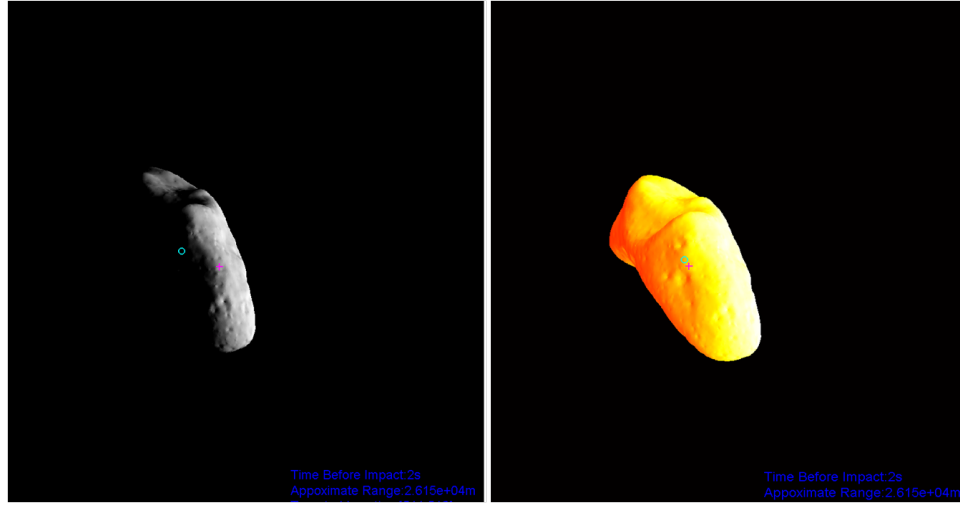


Figure 8. Comparison of an optical image model (left) and an IR image model (right).

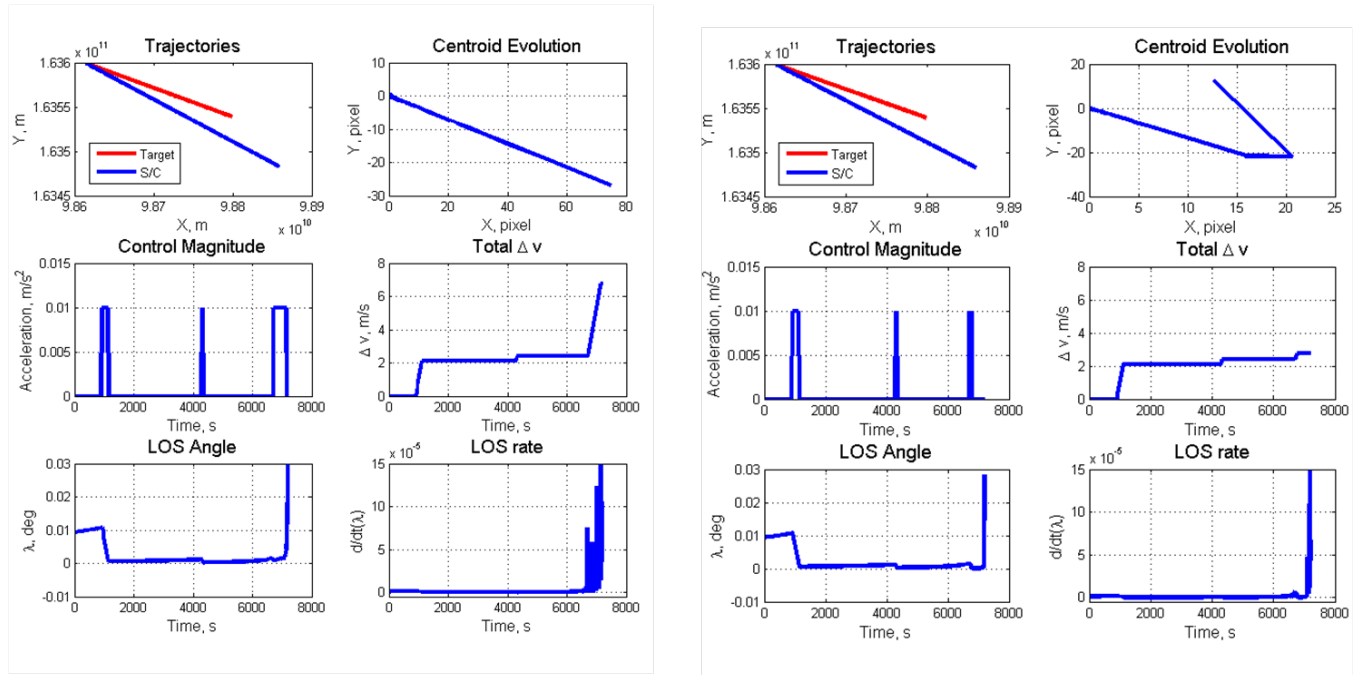


Figure 9. Terminal guidance performance comparison of an optical model (left) and an IR model (right).

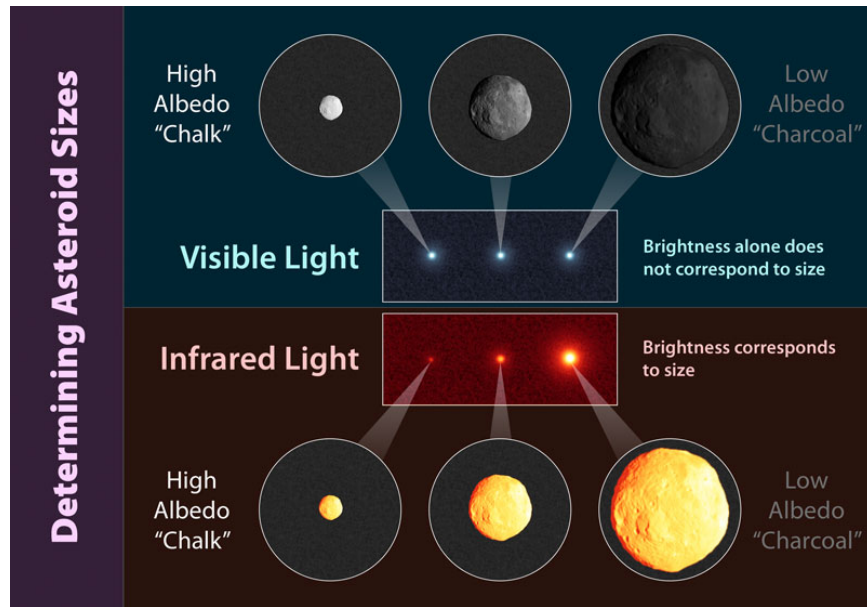


Figure 10. Comparisons of optical and infrared images of asteroids with different sizes and albedos. Image courtesy of http://wise.ssl.berkeley.edu/gallery_asteroid_sizes.html

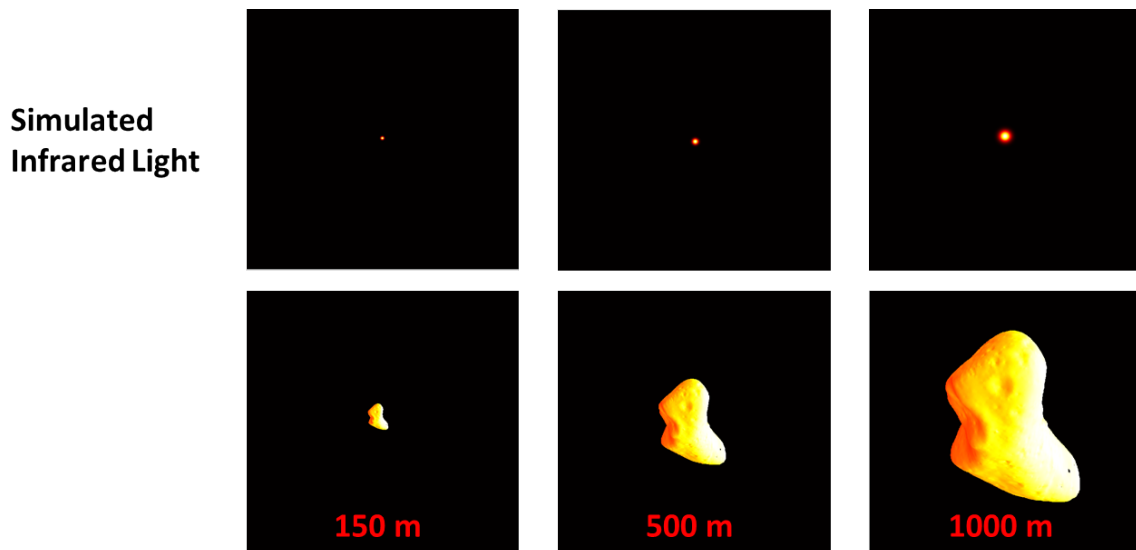


Figure 11. Asteroid infrared brightness and size comparison generated by in-house software being developed at the ADRC.

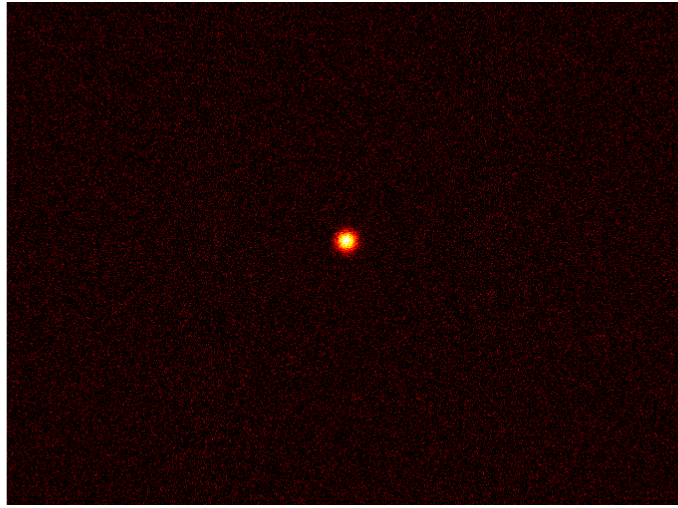


Figure 12. An illustrative IR sensor noise effect on an image of an asteroid.

Closed-loop terminal guidance simulation results are summarized in Figure 9. We notice that the total ΔV required to impact the target asteroid is less for the case with IR sensing than the case with optical sensing. This is due to the fact that the center of figure is very close to the center of mass, as illustrated in Figure 8. This near match may not always be the case, however. As the target's geometry changes, the separation distance between COF and COM may vary significantly.

For Figure 10, the ADRC's in-house GPU based guidance simulation program was used. For simplicity, pixel noise was not included in closed-loop terminal guidance simulation. An image of the sample target asteroid at a distance of 84,000 km is provided in Figure 12. This image includes representative noises in the sensor system. However, it is possible to reduce such sensor noise by utilizing a median filter with, possibly, a 3 pixel localization box. This subject will need a further study.

CONCLUSION

This paper has discussed a blended use of optical and infrared (IR) sensors for reliable target tracking and robust intercept of small (50 -150 m) asteroids. The technical feasibility of a closed-loop terminal guidance system employing both optical and IR sensors has been demonstrated. The preliminary study results indicated that it is possible to robustly track and intercept small (50 - 150 m) target asteroids using both optical and infrared sensors even under worst-case target illumination conditions. However, a further detailed study on the blended use of optical and infrared (IR) sensor fusion for hypervelocity asteroid intercept guidance is required.

ACKNOWLEDGMENT

This research was supported by a NIAC Phase 2 study entitled "An Innovative Solution to NASA's NEO Impact Threat Mitigation Grand Challenge and Its Flight Demonstration Mission Design." The authors would like to thank Dr. John Basart at Iowa State University for his technical advice on IR sensor modeling.

NOTATION

L	Radiance of Asteroid (W/m ² /sr.)
h	Planck's Constant (m ² kg/s)
c	Speed of Light in Vacuum (m/s)
λ	Wavelength of Radiation (m)
k_B	Boltzmann Constant (m ² kg/s ² /K)
ϵ	Emissivity of Object
τ_{optics}	Optics Transmission Coefficient
E	Irradiance (W/m ²)
N_p	Number of Photons per Second
Φ	Photon Flux (photons/m ² /sec)
I_{signal}	Signal Current (Amperes)
T_{ast}	Temperature of the Asteroid (K)
r_{ast}	Smallest Mean Radius of Asteroid (m)
R_{ast}	Distance from Sensor to Asteroid (m)
q	Charge of an Electron (coulombs)
η	Quantum Efficiency
G	Photoconductive gain of device
b	Wein's Displacement Constant (m K)
$n_{e,d}$	Dark Current for Detector (photons/pixel/ sec)
n_{pix}	Number of pixels
I_{dark}	Dark Current (Amperes)
I_J	Johnson Noise Current (Amperes)
I_S	Shot Noise Current (Amperes)
I_{GR}	Generation-Recombination Noise Current (Amperes)
l_x, l_y, l_z	Length, Width, and Thickness of Detector (m)
T_d	Temperature of the Detector (K)
\bar{I}	Average Current of the System (Amperes)
A_d	Area of the Detector's Face (m ²)
ν	Frequency (Hz)
F_{object}	General Flux Density for an Object (W/m ² /Hz)
F_{ast}	Flux Density for an Asteroid (W/m ² /Hz)
$F_{Gliese581c}$	Flux Density for Alpha Centauri A (W/m ² /Hz)
$m_{Gliese581c}$	Magnitude of Alpha Centauri A in IR
m_{ast}	Magnitude of an Asteroid in IR

REFERENCES

- [1] Wie, B. "Hypervelocity Nuclear Interceptors for Asteroid Disruption," Acta Astronautica, 90, 2013, pp. 146-155.
- [2] Pitz, A., Kaplinger, B., Vardaxis, G., Winkler, T., and Wie, B., "Conceptual Design of a Hypervelocity Asteroid Intercept Vehicle (HAIV) and Its Flight Validation Mission," Acta Astronautica, 94, 2014, pp. 42-56.
- [3] Barbee, B., Wie, B., Steiner, M., and Getzandanner, K., "Conceptual Design of HAIV Flight Demonstration Mission," AIAA-2013-4544, AIAA Guidance, Navigation, and Control Conference, Boston, MA, August 19-22, 2013.
- [4] Lyzhoft, J., Hawkins, M., Kaplinger, B., and Wie, B., "GPU-Based Optical Navigation and Terminal Guidance Simulation of a Hypervelocity Asteroid Impact Vehicle (HAIV)," AIAA-2013-4966, AIAA Guidance, Navigation, and Control Conference, Boston, MA, August 19-22, 2013.

- [5] Kaplinger, B., Wie, B., and Dearborn, D., "Nuclear Fragmentation/Dispersion Modeling and Simulation of Hazardous Near-Earth Objects," *Acta Astronautica*, 90, 2013, pp. 156-164.
- [6] Thomas, P.C., et al., "Eros: Shape, Topography and Slope Processes," *Icarus*, Volume 155, pp. 18-37, 2002.
- [7] Gouraud, H. "Continuous Shading of Curved Surfaces," *IEEE Transactions on Computers*, Volume C-20 (6): pp. 623-629, 1971.
- [8] National Aeronautics and Space Administration, "Near Earth Asteroid Rendezvous (NEAR) Press Kit," http://www.nasa.gov/home/hqnews/presskit/1996/NEAR_Press_Kit/NEARpk.txt [cited 14 September 2013].
- [9] Cutri, R. M., et al., "Explanatory Supplement to the WISE Preliminary Data Release Products," http://wise2.ipac.caltech.edu/docs/release/prelim/exp_sup/wise_prelrel_toc.html [cited 29 July 2013].
- [10] Schott, J. R., *Remote Sensing: The Image Chain Approach*, 1st ed., Oxford University Press, New York, 1997, pp. 184.
- [11] Rieke, J. H., *Detection of Light: from the Ultraviolet to the Sub-millimeter*, 1st ed., Cambridge University Press, New York, 1994, pp. 56.
- [12] Mainzer, A. K., et al., "Preliminary Design of The Wide-Field Infrared Survey Explorer (WISE)," <http://arxiv.org/pdf/astro-ph/0508246.pdf>, [cited 22 July 2013].
- [13] Dereniak, E. L., Boreman, G. D., *Infrared Detectors and Systems*, John Wiley & Sons, New York, 1996, Ch. 5.
- [14] Beletic, J. W., et al., "Teledyne Imaging Sensors: Infrared imaging technologies for Astronomy & Civil Space," *SPIE Conference on Astronomical Instrumentation*, 70210H-1-14, 2008, pp. 1-14.
- [15] Morin, F. J., Miata, J. P., "Electrical Properties of Silicon Containing Arsenic and Boron," *Physical Review*, Vol. 96, No. 1, 1954, pp. 28-35.
- [16] Schneider, H., Liu, H. C., *Quantum Well Infrared Photodetectors*, Springer-Verlag Berlin Heidelberg, New York, 2007, Ch. 2.
- [17] Pederson, Shelsea A. "Simulations of Infrared Very Long Baseline Interferometry of the Exoplanets Gliese 581C and Gliese 581D," *Journal of the Southeastern Association for Research in Astronomy* 2.1 (2008): 55-58.